Journal of Alloys and Compounds 509 (2011) 8728–8737

Contents lists available at ScienceDirect

Journal of Alloys and Compounds

journal homepage: www.elsevier.com/locate/jallcom

Thermal oxidation and nitridation of sputtered Zr thin film on Si via N_2O gas

Yew Hoong Wong, Kuan Yew Cheong*

Energy Efficient & Sustainable Semiconductor Research Group, School of Materials and Mineral Resources Engineering, Engineering Campus, Universiti Sains Malaysia, 14300 Nibong Tebal, Seberang Perai Selatan, Penang, Malaysia

ARTICLE INFO

Article history:
Received 7 April 2011
Received in revised form 13 June 2011
Accepted 13 June 2011
Available online 17 June 2011

Keywords:
Sputtered Zr
Nitrous oxide
Oxidation
Nitridation
Metal-oxide-semiconductor

ABSTRACT

Formation of ZrO_2 by simultaneous thermal oxidation and nitridation in nitrous oxide of sputtered Zr on Si substrate is reported here for the first time. Sputtered Zr on Si substrate and followed by oxidation and nitridation in nitrous oxide ambient at 700 °C for various durations (5–20 min) have been systematically investigated. The structural and chemical properties of the samples were examined. Chemical depth profiles of the samples have been evaluated by X-ray photoelectron spectroscopy. Stoichiometric Zr–O (ZrO_2) and its interfacial layer consisted of mixed sub-stoichiometric Zr–O, Zr–N, Zr–Si–O, Si–N, and/or Si–O–N phases were identified. A possible model related to the oxidation and nitridation mechanisms has been proposed and explained. Supportive results related to the model were obtained by energy filtered transmission electron microscopy, X-ray diffraction, Raman spectroscopy and Fourier Transform infrared analysis.

© 2011 Elsevier B.V. All rights reserved.

1. Introduction

Drastic downscaling of Si-based metal-oxide-semiconductor (MOS) devices in ultra-large-scale integrated circuitry has pushed SiO_2 gate dielectric thickness to the order of nanometers [1–3]. According to the International Technology Roadmap for Semiconductors [4] and several reports [3,5,6], as the oxide is thinned down to 1.2 nm, current directly tunneling through the oxide may increase tremendously. In order to overcome the aforementioned problem, high dielectric constant (κ) gate has been proposed as an alternative gate dielectric. Numerous high κ materials (Ta_2O_5 [7], Y_2O_3 [8–10], La_2O_3 [11], Nd_2O_3 [12], Sc_2O_3 [13], HfO_2 [14–16], and ZrO_2 [3,6,14,15,17]) have been extensively investigated and reported. Of these high κ materials, ZrO_2 may be considered as a potential candidate for the near future generation technology nodes. In particular, ZrO_2 is having a higher κ value when compared with HfO_2 for both amorphous and crystalline thin films [14,15]. Moreover, ZrO_2 can be easily stabilized in the form of cubic or tetragonal polymorphs [3,17,18]. This may further enhance its effective κ value. Nonetheless, quality and properties of the film depend on the deposition technique as well as the initial thin film constitution [19,20]. Besides, interface properties of the film play a critical role in determining the electrical properties of the device [17,19].

According to a review [3], sputtering of metallic Zr in an inert gas ambient, followed by a thermal oxidation process are able to produce and control stoichiometry of the oxide. Some literatures have also reported that ZrO_2 thin films were successfully formed by a combination of Zr metal sputtering and oxidation process in oxygen ambient [6,21–24]. However, literatures have shown that an undesirable interfacial layer (IL) was inevitably formed during the oxidation process in oxygen ambient [25,26]. This is mainly due to oxygen diffusion to the Si surface or oxygen transport via vacancies in the film. With the undesirable IL, it reduces the capacitance of the MOS capacitor.

So far, researchers have reported on the effects of pre-treated Si substrate with N_2O and NH_3 gas in order to suppress formation of interfacial defect by controlling the growth of IL thickness [27,28]. Besides, post-deposition annealing of ZrO_2 film in nitrogen ambient was also studied in order to improve its electrical properties [29,30]. It was found that incorporation of nitrogen into the film may retard the growth of interfacial layer and improved electrical properties of the film. This improvement may be attributed to two factors. Firstly, the presence of nitrogen is postulated to passivate the oxygen vacancies by forming Zr–N, Si–N, and/or Si–O–N bonds, thus reducing amount of interfacial traps. In addition, these particular bonds are believed to effectively suppress crystallization that may enhance thermal stability of the film. Secondly, dangling bonds of Si surface may be passivated by the nitrogen-rich species generated during nitridation process [31].

In this paper, formation of ZrO_2 by simultaneous thermal oxidation and nitridation of sputtered Zr is proposed. This simultaneous process can be carried out in N_2O or NO ambient. When the gas is heated high enough, nitrogen, oxygen, and their related compounds are formed. The dominance of the oxidation and nitridation processes may depend on their respective reaction rate. Gas of NO

* Corresponding author. Tel.: +60 4 599 5259; fax: +60 4 594 1011.
E-mail address: cheong@eng.usm.my (K.Y. Cheong).

0925-8388/$ – see front matter © 2011 Elsevier B.V. All rights reserved.
doi:10.1016/j.jallcom.2011.06.041

is extremely toxic [32]. Hence, to perform a simultaneous thermal oxidation and nitridation on metallic Zr, N_2O gas is more appropriate and preferable due to its non-toxic property [32]. However, up to date, there is no report on the effects of either N_2O or NO gas on a sputtered Zr thin film on Si substrate. Therefore, this is the main objective of this manuscript to report on the effects of thermal oxidation and nitridation in N_2O ambient of a sputtered Zr/n-type Si system on their structural and chemical properties. Based on these results, a possible model related to the oxidation and nitridation mechanisms has been proposed.

2. Experimental details

n-Type Si substrates (⟨1 0 0⟩ oriented, 1–10 Ωcm) were first subjected to an ultrasonic and Radio Corporation of America (RCA) cleaning then followed by a HF dipping (1 HF: 50 H_2O) process to remove native SiO_2 from the surface. A 5-nm thick Zr film was deposited on the cleaned Si substrates by a RF sputtering system (Edwards Auto 500). During the sputtering process, working pressure, RF power, and inert Ar gas flow were configured at 1.2×10^{-7} Torr, 170 W, and 20 cm^3/min, respectively. The deposition rate was set at 2 Å/s. The initial thickness of Zr film was monitored by an in situ monitoring system in the RF sputtering system. The thickness was also re-measured by ellipsometer, to confirm the thickness. The thickness of Zr film was 5.00 ± 0.05 nm. After the deposition, samples were placed into a horizontal tube furnace and heated up from room temperature to 700 °C in an Ar flow ambient and the heating rate was set at 10 °C/min. Once the set temperature was achieved, N_2O gas was purged in with a flow rate of 150 mL/min for a set of durations (5, 10, 15, and 20 min). The samples were withdrawn from the furnace after the furnace was cooled down to room temperature in an Ar ambient. A simple qualitative cellophane tape adhesion test has been carried out to examine the adhesion quality of ZrO_2 on Si substrate and there was no peeling off issue arisen.

Evaluations of structural and chemical properties of the samples were carried out by various characterization techniques. Compositional and depth profile measurements of the films were conducted by an X-ray photoelectron spectroscopy (XPS) (Kratos Axis Ultra-DLD) with a monochromatic Al-K_α X-ray source ($h\nu$ = 1486.69 eV) operated at 150 W and a take-off angle of 0° with respect to surface normal. In order to perform a depth profiling analysis, a 5-kV Ar ion etching was used. The pressure of Ar in the analysis chamber was 3×10^{-7} Torr, while the area of analysis was $220 \times 220\ \mu m^2$. The chemical compositions of the films were obtained from a combination of wide and narrow scans. A wide scan was first performed with a passing energy of 160 eV for 9 min to determine the elemental chemical states. The core-level spectra that had been detected were Zr 3*d*, Si 2*p*, O 1*s*, N 1*s*, and C 1*s*. Subsequently, for a narrow scan, a passing energy of 20 eV for 5 min was used to scan through the binding-energy range of interest. The recorded C 1*s* peak due to the adventitious carbon-based contaminant on the surface, with respect to the literature value of 284.6 eV [33,34], was used as a reference to compensate for the charging effect of the XPS spectra. Surface charge and linear background were corrected with the help of CasaXPS software (version 2.3.15) before deconvolution of the XPS spectra was performed. The total concentration of an element (C_x) available in the investigated films was calculated based on the following equation [35–37]

$$C_x = \frac{I_x/S_x}{\sum_i I_i/S_i} \times 100 \quad (1)$$

where, I_x and I_i were peak intensity of the evaluated element and all other detected elements, respectively. S_x and S_i were sensitivity factor of the respective evaluated element and all other detectable elements. The sensitivity factor is dependent on XPS system. In this work, the sensitivity factors for Zr 3*d*, Si 2*p*, O 1*s*, N 1*s*, and C 1*s* were 2.576, 0.328, 0.78, 0.47, and 0.278, respectively.

Energy filtered transmission electron microscopy (EFTEM) (Zeiss Libra 200) was employed to analyze cross-sectional images of the films. Prior to this, a protective layer of resist was deposited on the top most layer of a sample. Then it was ion-milled by a focused ion beam system. The zone axis used for the imaging was [1 1 0] and the reciprocal lattice vectors were [0 0 1], [0 2 0], and [0 $\bar{1}$ 0]. Interplanar spacing, *d*, of the polycrystalline structure was measured from the EFTEM images with the assistance of ImageJ software, which gives the accuracy of measurements in three decimal places. Crystallinity of the films were characterized by X-ray diffraction (XRD) system (P8 Advan-Bruker) in a scan range of 2θ = 20–40° with step time of 71.6 s and step size of 0.0342°. Copper (Cu K_α) with wavelength (λ) of 1.5406 nm was used as X-ray source. Raman spectroscopy measurements (Jobin Yvon HR 800 UV) using an Ar^+ incident beam with wavelength of 514.5 nm, were conducted to ascertain the stability of chemical bonding upon thermal oxidation and nitridation process. Fourier Transform infrared (FTIR) (Pelkin Elmer Spectrum GX) analysis was performed to analyze the chemical functional groups of the films.

3. Results and discussion

3.1. XPS measurements

Based on wide scan of XPS, core-level spectra of Zr 3*d*, Si 2*p*, O 1*s*, and N 1*s* have been detected in all oxidized samples. Then narrow scan was performed for each element. Depth profiles of these elements as a function of etching time for each sample were obtained (Fig. 1(a)–(d)). It is observed that at earlier etching time, Zr and O are the dominant elements with atomic ratio of about 1:2. This indicates a stoichiometric ZrO_2 has been formed. Based on this justification, a layer of ZrO_2 located at the outmost layer of each samples has been identified and indicated in Fig. 1. Atomic percentage of both Zr and O elements are decreasing as the etching time is extended and their ratio is deviated from 1:2, until they are totally disappeared. This is the boundary of oxide and Si. Beyond this boundary, atomic percentage of Si is increased significantly; indicating the appearance of Si substrate. In between Si and ZrO_2 boundaries, an interfacial layer (IL) with a mixture of Zr, O, Si, and N have been detected. Detail analysis of the chemical compound of the IL was performed by narrow scan of XPS and it will be discussed in the subsequent paragraphs. The thickness of ZrO_2 and IL are depending on oxidation time. Based on the figure, thickness of ZrO_2 is marginally increased as the oxidation time increases. A minute variation has been detected from EFTEM images and these will be presented and discussed in later paragraphs. Distribution of nitrogen in terms of broadness, maximum atomic percent, and its location vary with samples. It is seen that sample oxidized for 5 min reveals the highest atomic percent (18.90 at%) of nitrogen. The nitrogen concentration is in the range of 18–19% and it is consistently detected even more than 3000s of etching time (not shown). With this observation, one may hypothesize that nitrogen is embedded deep into the Si substrate. However, this type of distribution does not observe for other oxidized samples (10–20 min). In these samples, nitrogen is accumulated at the interfacial layer with concentration of 1.98–2.20 at%, which is much lower than the concentration detected in 5-min oxidized sample. Among the three oxidized samples (10, 15, and 20 min), 15-min oxidized sample demonstrates the highest concentration of nitrogen (2.20 at%). For 10- and 20-min oxidized samples, concentration of nitrogen is 1.98 and 2.08 at%, respectively. This is in line with the trend of IL thickness with 15-min oxidized sample showing the thinnest layer.

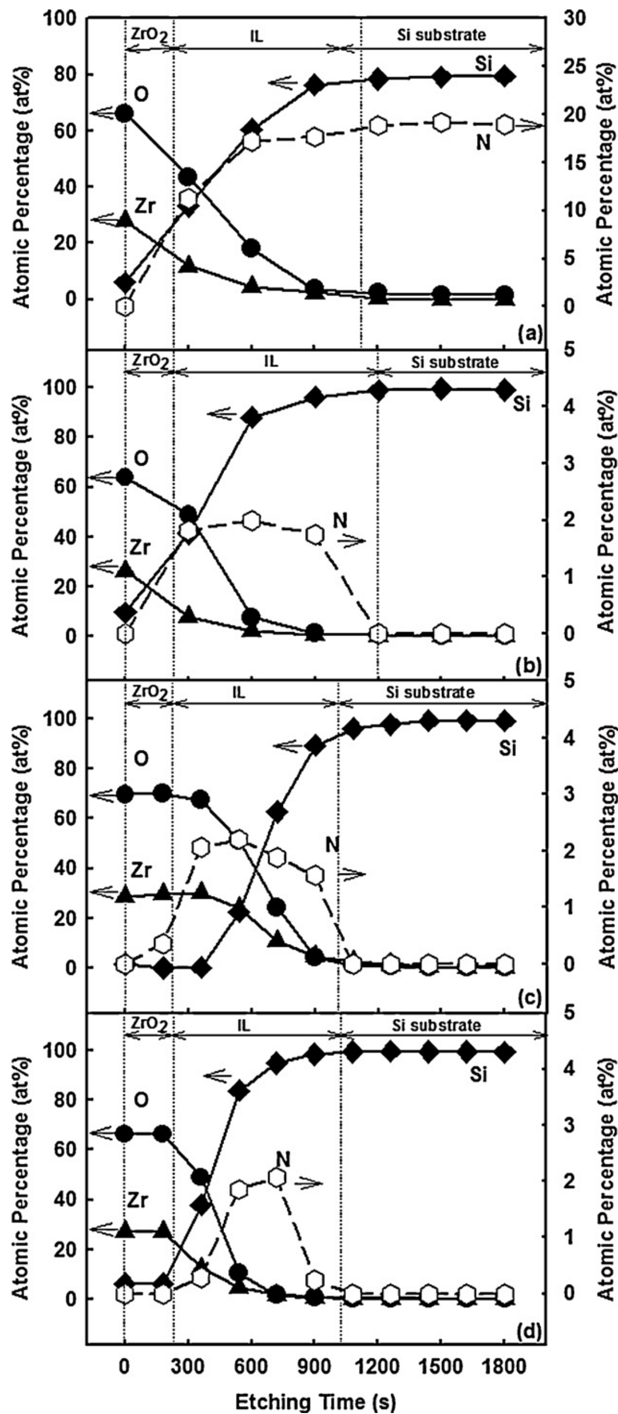

Fig. 1. Atomic percentage of Zr, Si, O, and N as a function of etching time for different oxidation duration samples: (a) 5 min, (b) 10 min, (c) 15 min, (d) 20 min.

Narrow scans of each core-level spectrum as a function of etching time for different oxidation durations (5–20 min) are presented in Figs. 2(a–d)–5(a–d). A non-linear Gaussian–Lorentzian function (solid lines) was employed to deconvolute the measured peaks (dotted lines) using CasaXPS software (version 2.3.15). The Zr 3*d* spectra (Fig. 2(a–d)) are well fitted by Zr–O, Zr–N, and/or Zr–Si–O components at their respective binding energies. Zr 3*d* doublet, which corresponds to $3d_{5/2}$ and $3d_{3/2}$ spin-orbit split components at 184.4 and 182.0 eV, respectively, has been detected at the top-most surface (etching time of 0 s) for all oxidized samples (5–20 min). This indicates that stoichiometric Zr–O (ZrO_2) is formed [38]. As the

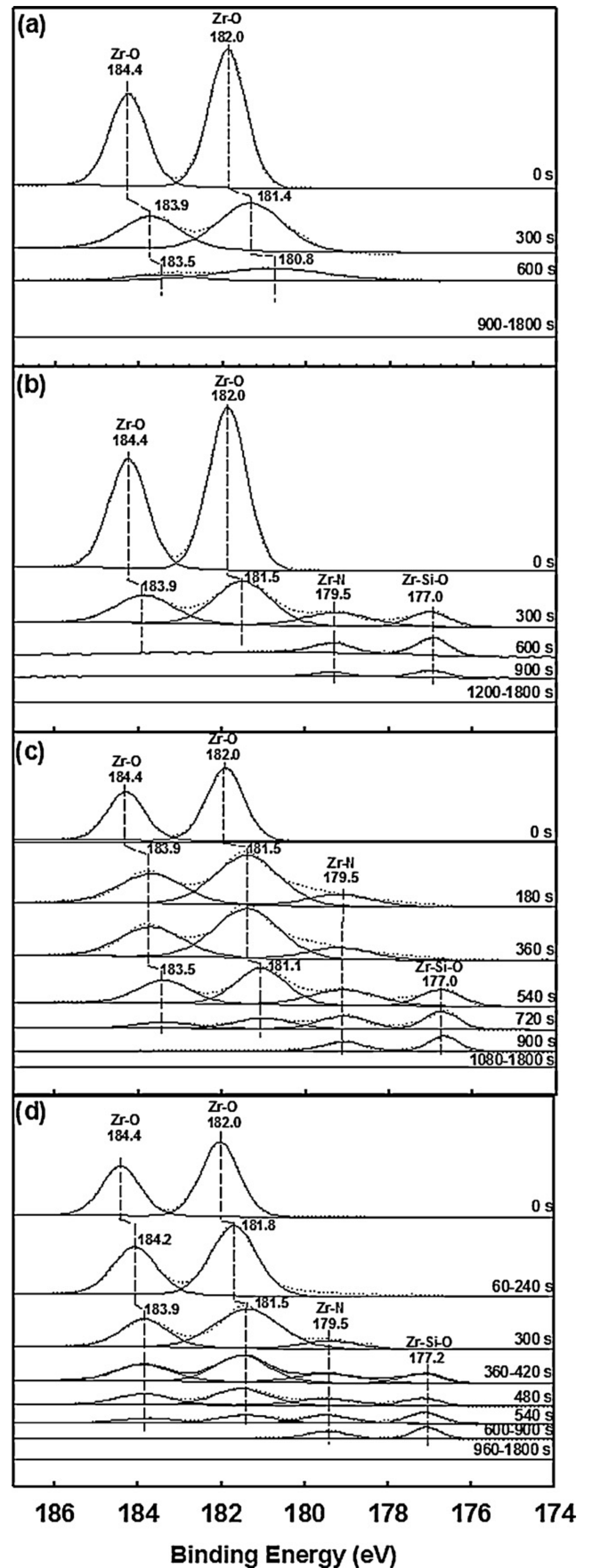

Fig. 2. Evolution of Zr 3*d* core level XPS spectra as a function of etching time for different oxidation duration samples: (a) 5 min, (b) 10 min, (c) 15 min, and (d) 20 min.

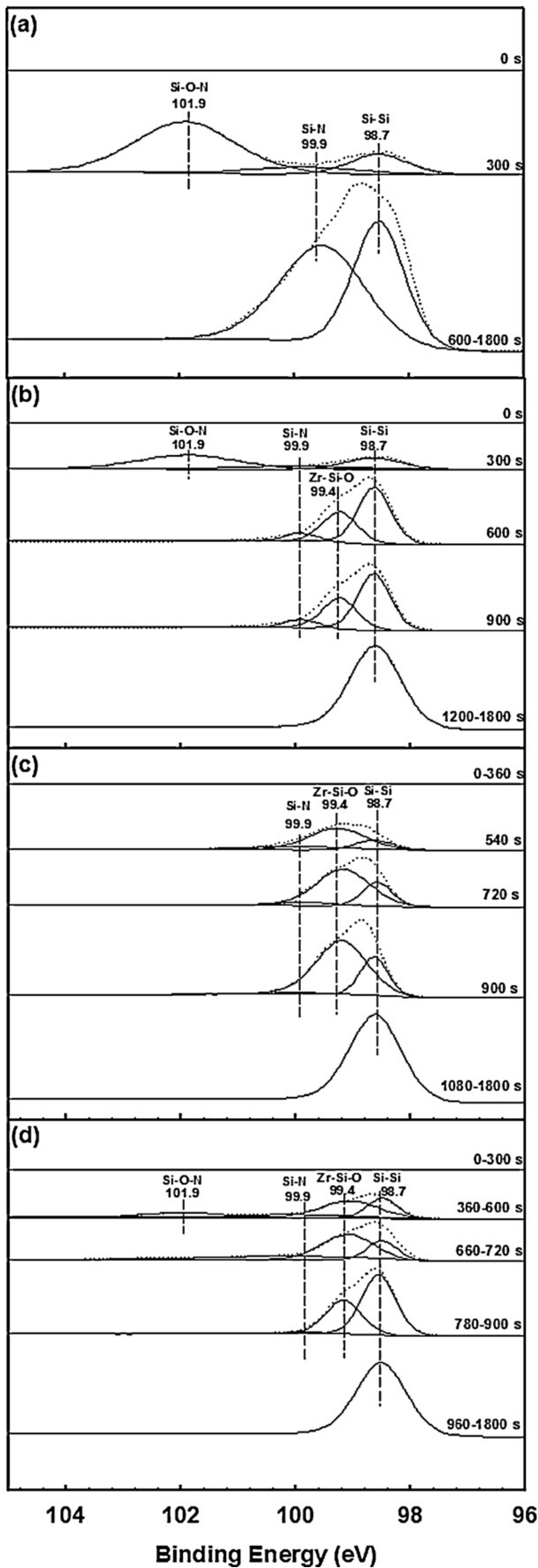

Fig. 3. Evolution of Si 2*p* core level XPS spectra as a function of etching time for different oxidation duration samples: (a) 5 min, (b) 10 min, (c) 15 min, and (d) 20 min.

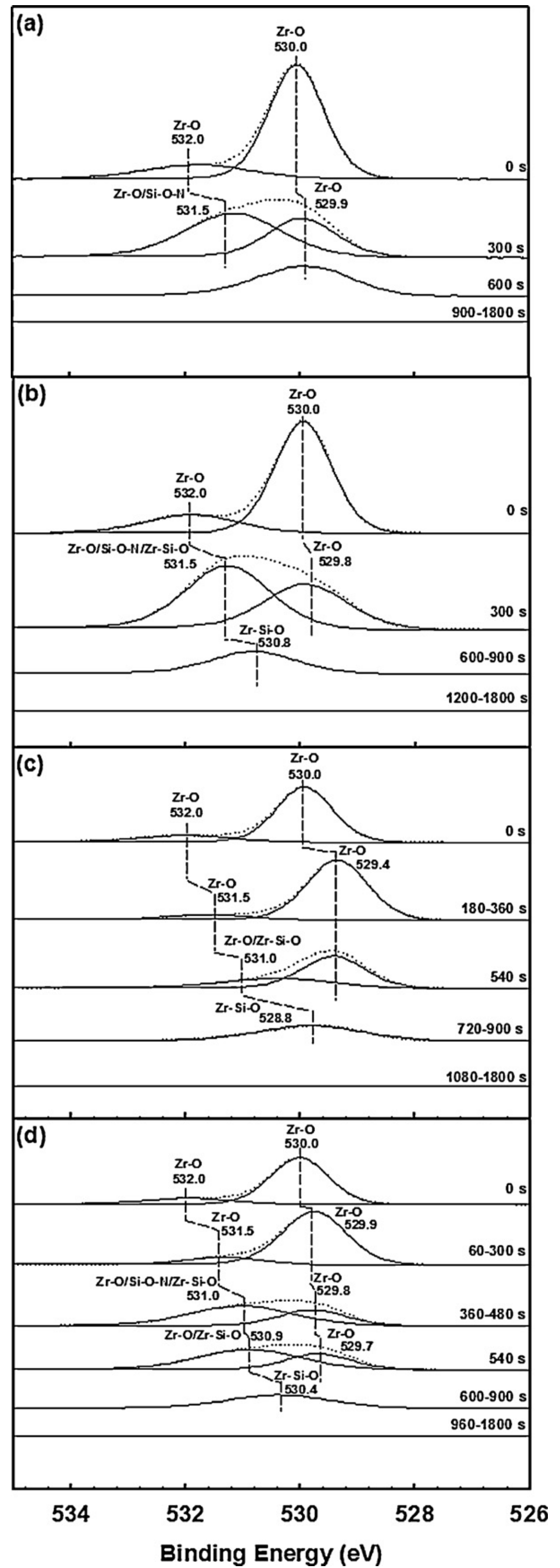

Fig. 4. Evolution of O 1*s* core level XPS spectra as a function of etching time for different oxidation duration samples: (a) 5 min, (b) 10 min, (c) 15 min, and (d) 20 min.

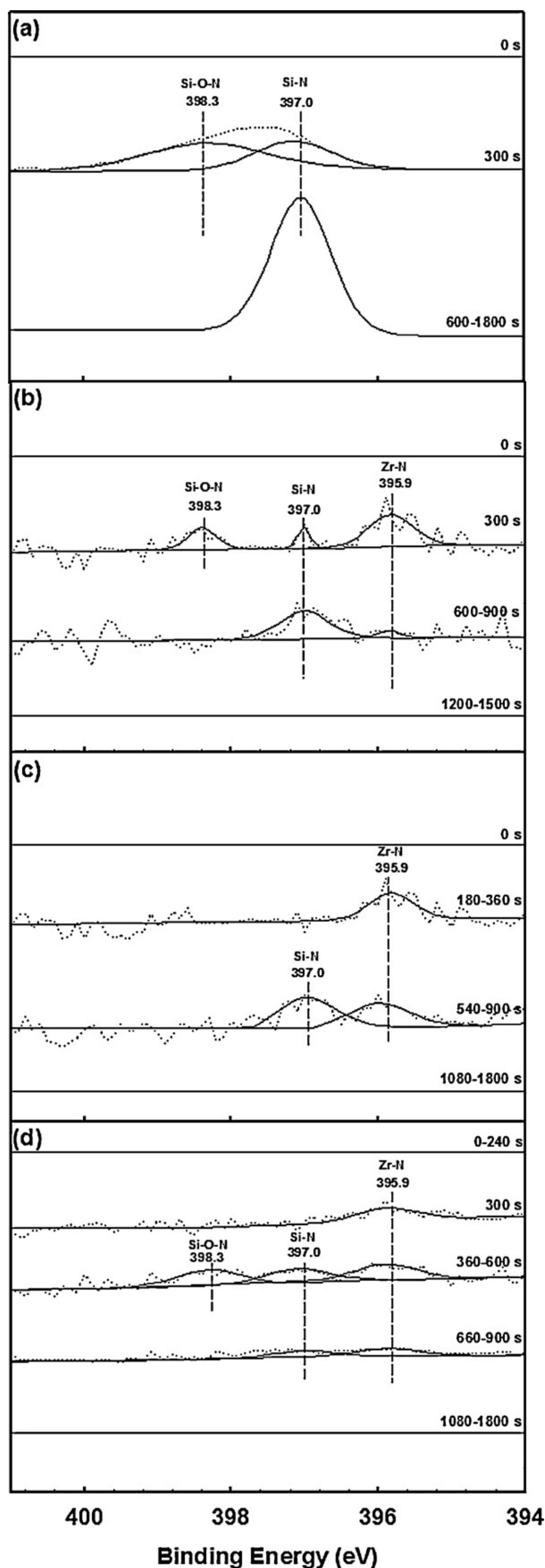

Fig. 5. Evolution of N 1*s* core level XPS spectra as a function of etching time for different oxidation duration samples: (a) 5 min, (b) 10 min, (c) 15 min, and (d) 20 min.

etching time increases, a progressive chemical shift of Zr–O peaks towards a lower binding energy has been observed. This is due to evolution from stoichiometric to sub-stoichiometric Zr–O towards a deeper region of all investigated films [39,40]. This is the only compound being detected in the 5-min oxidized sample. For samples with longer oxidation time (10–20 min), Zr–N (179.5 eV [41]) and Zr–Si–O (177.0 eV [22]) peaks can be matched; in addition to the Zr–O peak. This suggests that a region, which refers to IL, with Zr–O, Zr–N, and Zr–Si–O related compounds are presence. As the etching time increases and extended to Si substrate, intensity of Zr 3*d* spectra decreases and vanishes.

Si 2*p* spectra (Fig. 3(a–d)) were studied in order to further identify and verify existence of other components in the oxidized samples. Initially, there is no observable peak at the earlier etching time for all investigated samples. As the etching time increases, Si–O–N, Si–N, and/or Si–Si were detected at binding energies of 101.9 eV [35,37], 99.9 eV [37], and 98.7 eV [22,37,42], respectively. It is also noted that for 5-min oxidized sample, Si–N peak continues to be detected along with the Si–Si peak. The Si–Si peak is originated from Si substrate, while the Si–N peak may be associated to SiN_x compound. This result infers that SiN_x compound may be incorporated into the Si substrate for this particular sample. However, for other samples (10–20 min), the Si–N peak is not detectable in the Si substrate as this peak is vanished as the etching time is extended further. For all investigated samples, Si–O–N compound can be detected except for sample oxidized for 15 min. Intensity, which is indirectly related to the concentration of the related compound, is the highest for sample oxidized for 5 min, while the intensity is extremely low in samples oxidized for 10 and 20 min. Another detectable peak is associated with Zr–Si–O (99.4 eV [37]) for all investigated samples, except for 5-min oxidized sample. The intensity of this peak is reducing as the etching time is extended until it is totally vanished. The detection of this peak, with respect to the range of etching, is in consistent to the results shows in Zr 3*d* spectra (Fig. 2).

Analysis of O 1*s* spectra (Fig. 4(a–d)) is of particular interest as it depicts information, which was obtained earlier. At the top-most surface (etching time of 0 s) of all investigated films, two peaks can be fitted in the O 1*s* core level spectra. The peaks located at 530.0 eV [43,44] and 532.0 eV [45] are associated to stoichiometric Zr–O. Identical to the observation made in Zr 3*d* spectra (Fig. 2), the O 1*s* spectra has a progressive chemical shift towards lower binding energies. This is supported by the earlier claim (Fig. 2) that sub-stoichiometric Zr–O is detectable as it moves deeper inside. With increasing of etching time, Si–O–N (531.5 eV [35]) is detected in all oxidized samples, except in sample oxidized for 15 min. This is in agreement with the observation being obtained in Si 2*p* spectra (Fig. 3). Coincidently, this peak (531.5 eV) is overlapping with Zr–O that is chemically shifted due to non-stoichiometry. Another possible compound that could be fitted to 531.5 eV is Zr–Si–O [44]. Based on Guittet et al. [44], binding energy of Zr–Si–O in O 1*s* spectrum was at 531.3 eV. The existence of this compound is highly possible in samples oxidized for 10–20 min and it is unlikely to be detected in sample oxidized for 5 min. This is because this peak was not revealed in Zr 3*d* spectra (Fig. 2) for that particular sample. It has been reported that the occurrence of Zr–Si–O compound may be attributed to the depletion of oxygen [46].

Narrow scan of N 1*s* core level spectra is presented in Fig. 5(a–d). There is no peak being detected at earlier etching time. With the increment of etching time, a peak at binding energy at 398.3 eV is detected in all samples, except in sample oxidized for 15 min. This peak is associated with Si–O–N [35,47]. Again, this conclusion is in agreement with the analysis obtained from Si 2*p* spectra (Fig. 3). Si–N (397.0 eV [35,47]) is another weakly detected compound in all investigated samples. An exceptionally strong intensity of this peak has been revealed in sample oxidized for 5 min and it is

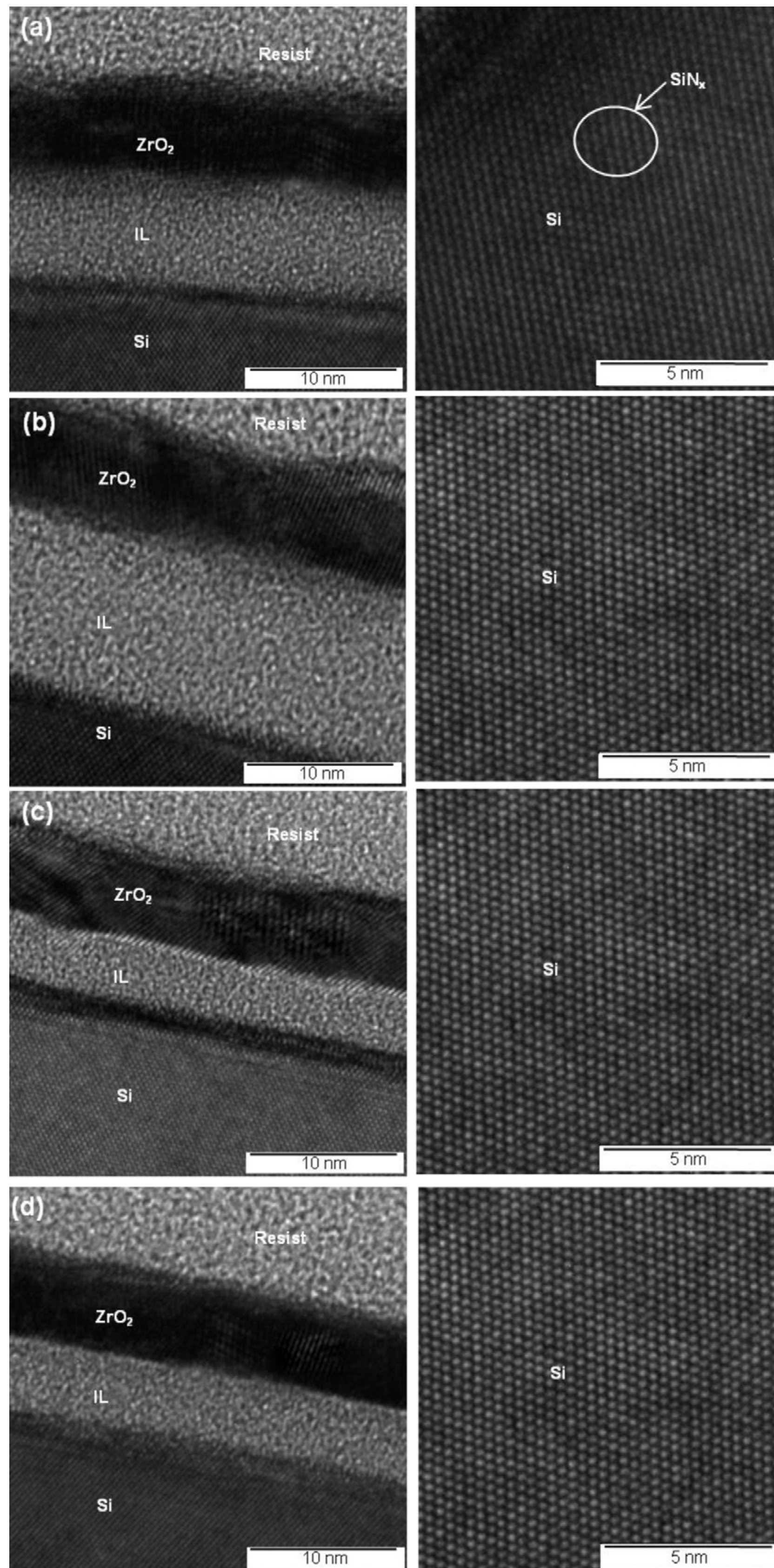

Fig. 6. Cross-sectional of EFTEM images of the investigated samples at different oxidation durations: (a) 5 min, (b) 10 min, (c) 15 min, and (d) 20 min. Magnified images of Si substrate of each of the investigated sample is shown on the right side respectively.

Table 1
Possible compounds in the interfacial layers of the investigated samples.

Compounds	Oxidation time (min)			
	5	10	15	20
Sub-stoichiometric Zr–O	√	√	√	√
Si–O–N	√	√		√
Si–N	√	√	√	√
Zr–N		√	√	√
Zr–Si–O		√	√	√

located deep inside Si substrate (etching time of 600 s and beyond) (Fig. 5(a)) as what has been shown in the nitrogen profile in Fig. 1(a). To support the fitting of Zr–N in Zr 3*d* spectra (Fig. 2), peak related to this compound can be identified at binding energy of 395.9 eV [34] for all investigated samples, except for 5-min oxidized sample. Based on the analyses of the Zr 3*d*, Si 2*p*, O 1*s*, and N 1*s* spectra in Figs. 2–5, possible compounds being detected in interfacial layers of the investigated samples are shown in Table 1.

3.2. EFTEM analysis

From the cross-sectional EFTEM images (Fig. 6), stoichiometric ZrO_2 in polycrystalline structure has been revealed for all investigated sample, as patches of lattice fringes can be clearly seen with interplanar spacing, *d*, of 0.260–0.300 nm. This value was measured from the images and it is in agreement with the *d* value of ZrO_2 [48,49]. The measured physical thickness of ZrO_2 is approximately 6 nm for all investigated samples and the thickness is marginally increased as the oxidation time increases (Fig. 7). This is due to longer oxidation time that allows oxygen to diffuse in deeper and reacts with Zr. In contrast, thickness of interfacial layer varies with oxidation time. These results are supportive to the chemical depth profile analysis in Fig. 1.

From Fig. 6, it is observed that there is a layer between the Si substrate and the interfacial layer in all oxidized samples. This layer is regarded as one of the interfacial layers. Based on the summarized analysis in Table 1, interfacial layers may comprise of sub-stoichiometric Zr–O, Zr–Si–O, Zr–N, Si–O–N, and Si–N, depending on the oxidation time. The interfacial layers are in amorphous structure (Fig. 6). As shown in Fig. 7, effective thickness of interfacial layer in 15-min oxidized samples is approximately 4.0 nm and in 10-min oxidized sample is approximately 10.0 nm with the thickness of other samples in between this range.

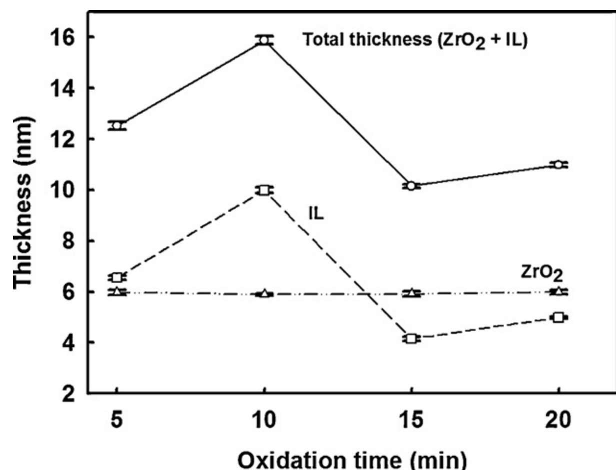

Fig. 7. Average thicknesses of ZrO_2 and interfacial layers for the investigated samples. Error bars define the maximum and minimum thicknesses obtained.

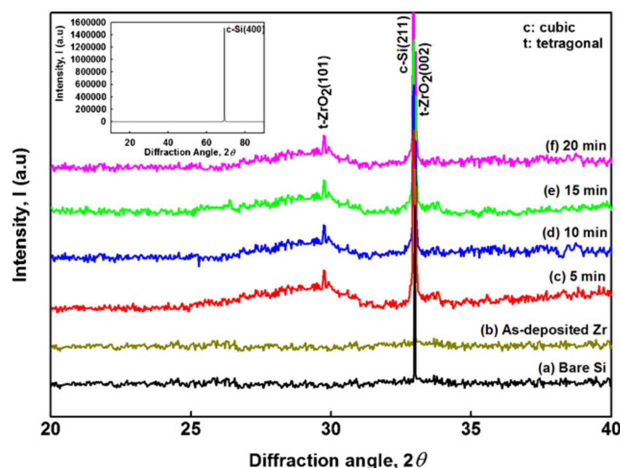

Fig. 8. XRD patterns of bare n-type Si substrate, as-deposited Zr on Si, and oxidized samples at 700 °C for various oxidation times (5–20 min). Inset shows c-Si(4 0 0) peak with very strong intensity at 69.0°.

From the magnified images of Si substrate (Fig. 6), it is noticeable that in 5-min oxidized sample, a slight expansion in the interplanar spacing of Si substrate. According to the XPS results in Fig. 5(a), Si–N is detected in Si substrate. Incorporation of nitrogen in Si substrate may form nanocrystallite SiN_x. The lattice constant of SiN_x is larger (a = 0.56217 nm [50]) than the constant of Si substrate (a = 0.54300 nm [3]). Therefore, an expansion is observed.

3.3. XRD analysis

Fig. 8(a–f) shows the XRD patterns of bare *n*-type Si substrate, as-deposited Zr on Si, and oxidized samples for different durations. A very strong intensity of diffraction peak at 69.0° (inset of the figure) is recorded in all investigated samples and the peak is matched with c-Si(4 0 0). In additional, a minor peak at diffraction angle (2θ) of 33.1° is also detected and it is matched with c-Si(2 1 1) as confirmed by The International Conference for Diffraction Data (ICDD) card number 01-089-2749 and 01-072-1426, respectively.

Due to amorphous structure of sputtered metallic Zr on Si, no diffraction peak is detected in pattern (b) of Fig. 8. After oxidation, t-ZrO_2(1 0 1) and t-ZrO_2(0 0 2) are revealed at diffraction angle of 29.8° and 33.3° (ICDD: 00-024-1164), respectively, for all oxidized films (Fig. 8(c–f)). According to the ICDD file (00-024-1164), interplanar spacing of t-ZrO_2(1 0 1) and t-ZrO_2(0 0 2) are 0.2995 nm and 0.2635 nm, respectively. Therefore, from the XRD analysis, it suggests that crystalline t-ZrO_2 is formed and the result is supported by the measured interplanar spacing obtained from EFTEM images (Fig. 6).

3.4. Raman spectroscopy

Since no direct indication of t-ZrO_2 stabilization is produced in the XRD spectra, Raman spectroscopy has been employed to determine the stabilization of t-ZrO_2 upon thermal oxidation and nitridation process. The Raman results for all investigated samples (5–20 min) are demonstrated in Fig. 9(a)–(d). Three peaks located at 300 cm^{-1} [51], 430 cm^{-1} [51], and 520 cm^{-1} [52] are originated from the silicon substrate in all investigated samples. On the other hand, presence of a peak at 250 cm^{-1} [51] is identified to be t-ZrO_2 in all investigated samples. Based on this result, it has confirmed that a stable t-ZrO_2 has been formed in all investigated samples, complementing with the findings provided by XRD analysis.

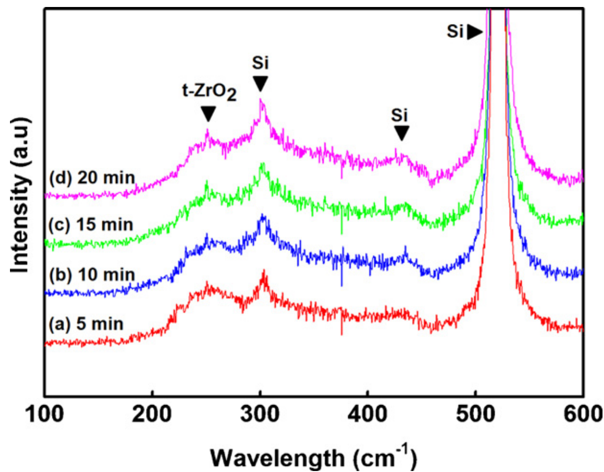

Fig. 9. Raman spectra of oxidized samples at 700 °C for various oxidation durations (5–20 min).

3.5. FTIR analysis

FTIR analysis was carried out in order to further identify the chemical functional groups in the samples. Fig. 10 displays the FTIR transmittance spectra (1200–400 cm^{-1}) of bare n-type Si substrate, as-sputtered Zr on Si, and oxidized samples for various oxidation time. Si–Si vibration mode band, which is originated from Si substrate, is located at 610 cm^{-1} in all samples. Sample of as-sputtered Zr on Si does not show any detectable peak of Zr–Zr and/or Zr–Si. This is because those inorganic bonds are inactive in region of mid-infrared (4000–400 cm^{-1}) [53,54]. For oxidized samples, transmittance bands of Zr–O vibration mode are detected at around 440 and 580 cm^{-1} and it is associated with ZrO_2 [55–58]. Besides, a band at 1100 cm^{-1} is recorded in all investigated samples. This band is related to Si–O bond in Zr–O–Si stretching vibration or in Si–O–N vibration [56,59,60]. These results are complementary with the conclusions based on XPS and XRD.

3.6. Oxidation and nitridation mechanisms

From the structural and chemical characterizations, a possible model of oxidation and nitridation mechanisms of sputtered Zr in N_2O ambient has been proposed (Fig. 11). Due to fast initial oxidation of Zr at room temperature, a very thin monolayer (~1 nm) of

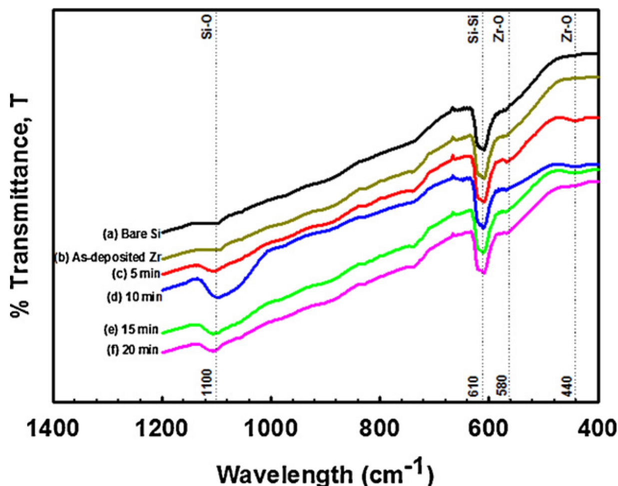

Fig. 10. FTIR transmittance spectra for bare n-type Si substrate, as-deposited Zr on Si, and oxidized samples at 700 °C for various oxidation durations (5–20 min).

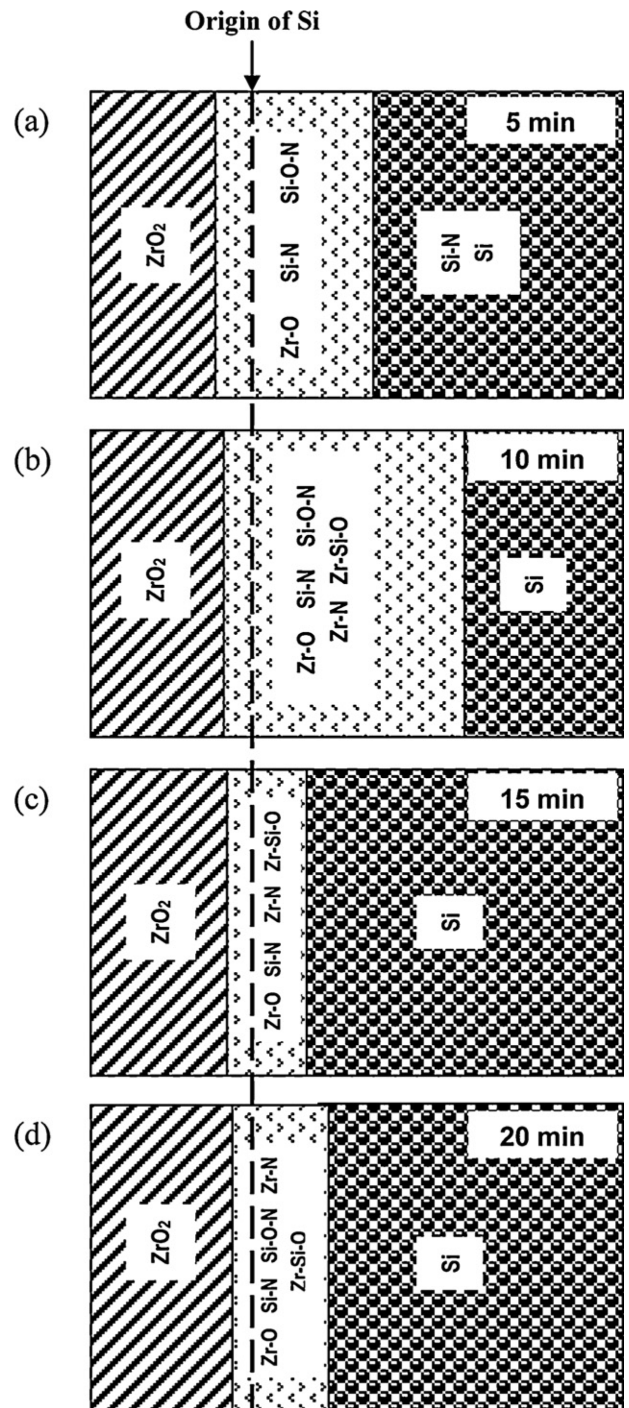

Fig. 11. Model of layers distribution after different oxidation time: (a) 5 min, (b) 10 min, (c) 15 min, (d) 20 min.

ZrO_2 is formed on the top-most surface according to the following reaction [61]:

$$Zr + O_2 \rightarrow ZrO_2 \quad (2)$$

According to the experimental works carried out by Gupta et al. [62] and Enta et al. [32], decomposition of N_2O was at elevated temperatures above 1000 °C. Nevertheless, based on the study conducted by Miller and Grassian [63], it was determined that ZrO_2 is an effective catalyst for the decomposition of N_2O, whereby N_2O will decompose exclusively to N and O compounds. The study was also identified that Zr cations were involved in the decomposition

reaction of N_2O. As reported by Zhu et al. [64], a complete catalytic decomposition of N_2O on ZrO_2 happens at temperature of 700 °C, therefore, this particular temperature was chosen in this study. It is reported by Petrucci et al. [65] that there is no free energy change-temperature dependence in the decomposition of N_2O into N and O compounds. Therefore, the decomposition is spontaneous at all reaction temperatures.

During initial stage (5 min), Zr cations as catalytic ions are able to decompose N_2O into N and O compounds. The decomposition rate is higher in this stage than other extended oxidation time. As the oxidation time is extended, less Zr cations acting as catalyst are remained in the system and therefore, less N and O compounds are produced. Since oxygen atoms are easily being sensed and absorbed by Zr metal [66], the absorbed O atoms may react with Zr to form Zr–O compound. This process may proceed further inward, depending on the availability of oxygen. The reaction is described by:

$$\overrightarrow{O} + Zr \rightarrow Zr\text{–}O \quad (3)$$

where, the arrow pointing to the right above a chemical symbol indicates an inward diffusion process of the particular chemical. A stoichiometric Zr–O (ZrO_2) layer is formed, when sufficiently high concentration of oxygen is supplied [66]. As the thickness of ZrO_2 increases, less oxygen may diffuse in and cause an incomplete reaction between Zr and O. As a result, a sub-stoichiometric Zr–O compound is formed at interfacial layer between the stoichiometric Zr–O compound (ZrO_2) and the Si substrate.

Concurrently, nitridation process is also taking place, in which inward diffusing N atoms may either react with outward diffusing Si atoms originated from Si substrate or with static Si atoms of the substrate. Either possibility may form Si–N:

$$\overrightarrow{N} + \leftarrow Si \ \text{ or } \ Si \rightarrow Si\text{–}N \quad (4)$$

where, the arrow pointing to the left above a chemical symbol indicates an outward diffusion of that particular chemical. When nitrogen atoms react with out-diffusing Si atoms, Si–N related compound is formed at the interfacial layer. While the reaction between nitrogen and static Si substrate may form nanocrystalline of SiN_x. Based on EFTEM analysis (Fig. 6(a)), the nanocrystalline is embedded in Si substrate. Formation and embedment of the nanocyrstalline can be explained as follows. During initial decomposition of N_2O, high concentration of nitrogen is produced due to higher amount of Zr cations, which is acting as catalytic ions [nitrogen profile in Fig. 1(a)]. Since the concentration of nitrogen is high, it may easily diffuse towards the Si substrate. In addition to that, due to the smaller atomic size of nitrogen than oxygen; hence, nitrogen is easier to diffuse deeper into Si substrate. The diffused nitrogen is trapped in the substrate when the oxidation process is terminated at 5 min. The trapped nitrogen may spontaneously react with Si to form nanocrystalline of SiN_x. Based on these explanations, it is concluded that the nitridation rate is higher than oxidation rate for sample oxidized for 5 min.

Simultaneously, excessive diffusing O and N atoms may react with out-diffusing Si atoms to form Si–O–N at the interfacial layer [35,67]:

$$\leftarrow Si + \overrightarrow{O} + \overrightarrow{N} \rightarrow Si\text{–}O\text{–}N \quad (5)$$

As the oxidation time is extended to 10 min, less N_2O can be decomposed. This is attributed to the initial ZrO_2 layer being formed at 5 min oxidation acting as a barrier layer or caused by less availability of Zr cations acting as catalyst. Owing to this, only a marginal increment in ZrO_2 thickness is observed (Fig. 7). Due to the extended oxidation time, oxygen is able to diffuse in deeper and react with Zr. However, the amount of oxygen is relatively low. Hence, reaction between Zr and O may be uncompleted and sub-stoichiometric Zr–O is formed at the interfacial layer. Simultaneously, owing to the out-diffusion of Si atom and reaction with the sub-stoichiometric Zr–O, Zr–Si–O compound may be formed [43,68–71]:

$$Zr\text{–}O + \overrightarrow{O} + \leftarrow Si \rightarrow Zr\text{–}Si\text{–}O \quad (6)$$

$$Zr\text{–}O + \leftarrow Si \rightarrow Zr\text{–}Si\text{–}O \quad (7)$$

Similarly, amount of nitrogen that is diffusing inwards is also less (nitrogen profile in Fig. 1) due to lesser Zr cations, as catalyst, and thicker ZrO_2, as barrier layer. The concentration of nitrogen is much lower than the pre-existing concentration of nitrogen trapped in Si substrate. Due to this, a concentration gradient of nitrogen is created and out-diffusion of nitrogen from the Si substrate towards the interface layer is initiated. The out-diffusing nitrogen may react with sub-stoichiometric Zr–O to form Zr–N compound by releasing oxygen [72]:

$$Zr\text{–}O + \overrightarrow{N} \rightarrow Zr\text{–}N + O \quad (8)$$

The reported Gibbs free energies of formation of ZrN and stoichiometric ZrO_2 at 700 °C are −403.27 kJ/mol [65,72,73] and −1146.14 kJ/mol [65,72,74], respectively. This indicates the formation of ZrN is less favourable than formation of stoichiometric ZrO_2 at this temperature. However, in this case, the Zr–O involved is sub-stoichiometric, therefore, the formation of ZrN (Eq. (8)) is more favourable. Simultaneously, the nitrogen may also react with out-diffusing Si to form Si–N. Since the supply of oxygen is coming from in-diffusion of the decomposed N_2O and from dissociation of sub-stoichiometric Zr–O (Eq. (3)), it may react with Si–N to form Si–O–N compound [35,67]. In this situation, it is proposed that the oxidation rate is higher than nitridation rate.

When the oxidation time is prolonged to 15 min (Fig. 10(c)), Si–O–N is absent. This is because Si–O–N is re-structured to form a more thermodynamically stable Si–N compound [35,67]:

$$Si\text{–}O\text{–}N \rightarrow Si\text{–}N + \leftarrow O \quad (9)$$

During this reaction, oxygen is released and together with oxygen from the ambient, sub-stoichiometric Zr–O (Eq. (3)) and Zr–Si–O (Eqs. (6) and (7)) compounds are produced and enhanced. The out-diffusion of nitrogen is continued to happen and it is further reacted with sub-stoichiometric Zr–O to form Zr–N (Eq. (8)). Therefore, the concentration of Zr–N is increased if compared with sample oxidized for 10 min. With the re-structuring of Si–O–N to Si–N (Eq. (9)), thickness of interfacial layer is reduced. For this duration of process (15 min), oxidation and nitridation rates are in equilibrium.

As the oxidation time is extended to 20 min, available compounds in the interface layer are further re-structured. Concurrently, Si–O–N is re-formed and a slight increment in the interfacial thickness is observed. The formation of Si–O–N may attribute to the higher oxidation rate than nitridation rate. Based on this model, formation of ZrO_2 and compounds related to interfacial layers of all oxidized samples has been explained.

4. Conclusions

In this work, structural and chemical properties of sputtered Zr oxidized in N_2O ambient for different oxidation durations (5–20 min) were presented. Based on XPS results, the oxidized and nitrided layers consisted of a stacked stoichiometric Zr–O (ZrO_2) layer on an interfacial layer with compounds related to sub-stoichiometric Zr–O, Zr–N, Zr–Si–O, Si–N, and/or Si–O–N. A possible model related to the oxidation and nitridation mechanism has been proposed and explained. EFTEM images illustrated that a polycrystalline ZrO_2 had been formed along with the amorphous interfacial layers in the sample. This result is then further supported by XRD analysis and Raman spectroscopy, concluding that the ZrO_2 was in

tetragonal phase. FTIR analysis was used to identify chemical functional groups of the samples. It indicated that Zr–O and Zr–Si–O were formed in the oxidized films. The reported structural and chemical properties of the film in this study may serve as a key role to understand the functional properties of the film to work as advanced high-κ dielectric in MOS-based devices.

Acknowledgements

The authors would like to acknowledge USM fellowship, USM-RU-PRGS (8032051) and The Academy Sciences for the Developing World (TWAS) through TWAS-COMSTECH Research Grant (09-105 RG/ENG/AS_C) for the financial support during the study.

References

[1] J. Robertson, Eur. Phys. J. Appl. Phys. 28 (2004) 265–291.
[2] G.D. Wilk, R.M. Wallace, J.M. Anthony, J. Appl. Phys. 89 (2001) 5243–5275.
[3] Y.H. Wong, K.Y. Cheong, J. Mater. Sci.: Mater. Electron. 21 (2010) 980–993.
[4] http://www.itrs.net/Links/2009ITRS/Home2009.htm, International Technology Roadmap for Semiconductors (ITRS) 2009, accessed August 2010.
[5] H.J. Quah, K.Y. Cheong, Z. Hassan, Z. Lockman, F.A. Jasni, W.F. Lim, J. Electrochem. Soc. 157 (2010) H6–H12.
[6] T. Kurniawan, K.Y. Cheong, K.A. Razak, Z. Lockman, N. Ahmad, J. Mater. Sci.: Mater. Electron. 22 (2011) 143–150.
[7] C.J. Huang, Thin Solid Films 478 (2005) 332–337.
[8] W.M. Cranton, D.M. Spink, R. Stevens, C.B. Thomas, Thin Solid Films 226 (1993) 156–160.
[9] K.-H. Kwon, C.K. Lee, J.-K. Yang, S.G. Choi, H.J. Chang, H. Jeon, H.-H. Park, Microelectron. Eng. 85 (2008) 1781–1785.
[10] H.J. Quah, W.F. Lim, S.C. Wimbush, Z. Lockman, K.Y. Cheong, Electrochem. Solid-State Lett. 13 (2010) H396–H398.
[11] Y.H. Wu, M.Y. Yang, A. Chin, W.J. Chen, C.M. Kwei, IEEE Electron. Device Lett. 21 (2000) 341–343.
[12] C.-H. Kao, T.C. Chan, K.S. Chen, Y.-T. Chung, W.-S. Luo, Microelectron. Reliab. 50 (2010) 709–712.
[13] C.P. Chen, M. Hong, J. Kwo, H.M. Cheng, Y.L. Huang, S.Y. Lin, J. Chi, H.Y. Lee, Y.F. Hsieh, J.P. Mannaerts, J. Cryst. Growth 278 (2005) 638–642.
[14] D.M. Hausmann, R.G. Gordon, J. Cryst. Growth 249 (2003) 251–261.
[15] G.M. Rignanese, X. Gonze, G. Jun, K. Cho, A. Pasquarello, Phys. Rev. B 69 (2004) 184301.
[16] K.S. Park, K.H. Baek, D.P. Kim, J.C. Woo, L.M. Do, K.S. No, Appl. Surf. Sci. 257 (2010) 1347–1350.
[17] W. Weinreich, V.A. Ignatova, L. Wilde, S. Teichert, M. Lemberger, A.J. Bauer, R. Reiche, E. Erben, J. Heitmann, L. Oberbeck, U. Schroder, J. Appl. Phys. 106 (2009) 034107–34117.
[18] I. Jõgi, K. Kukli, M. Ritala, M. Leskelä, J. Aarik, A. Aidla, J. Lu, Microelectron. Eng. 87 (2010) 144–149.
[19] G. Aygun, I. Yildiz, J. Appl. Phys. 106 (2009) 014312–14317.
[20] W.F. Lim, K.Y. Cheong, Z. Lockman, J. Alloys Compd. 497 (2010) 195–200.
[21] L.-Z. Hsieh, H.-H. Ko, P.-Y. Kuei, C.-Y. Lee, Jpn. J. Appl. Phys. 45 (2006) 7680–7681.
[22] H.D. Kim, S.W. Jeong, M.T. You, Y. Roh, Thin Solid Films 515 (2006) 522–525.
[23] Y. Nagasato, T. Aya, Y. Iwazaki, M. Hasumi, T. Ueno, K. Kuroiwa, Jpn. J. Appl. Phys. 44 (2005) 5–7.
[24] T. Kurniawan, Y.H. Wong, K.Y. Cheong, J.H. Moon, W. Bahng, K. Abdul Razak, Z. Lockman, H. Joon Kim, N.-K. Kim, Mater. Sci. Semicond. Process 14 (2011) 13–17.
[25] H. Watanabe, Appl. Phys. Lett. 83 (2003) 4175–4177.
[26] S. Ferrari, G. Scarel, J. Appl. Phys. 96 (2004) 144–149.
[27] L.-M. Chen, Y.-S. Lai, J.S. Chen, Thin Solid Films 515 (2007) 3724–3729.
[28] J.H. Choi, Y. Mao, J.P. Chang, Mater. Sci. Eng. R. 72 (2011) 97–136.
[29] Y.S. Lin, R. Puthenkovilakam, J.P. Chang, C. Bouldin, I. Levin, N.V. Nguyen, J. Ehrstein, Y. Sun, P. Pianetta, T. Conard, W. Vandervorst, V. Venturo, S. Selbrede, J. Appl. Phys. 93 (2003) 5945–5952.
[30] L.Q. Zhu, Q. Fang, G. He, M. Liu, L.D. Zhang, Mater. Lett. 60 (2006) 888–891.
[31] R.M.C. de Almeida, I.J.R. Baumvol, Surf. Sci. Rep. 49 (2003) 1–114.
[32] Y. Enta, K. Suto, S. Takeda, H. Kato, Y. Sakisaka, Thin Solid Films 500 (2006) 129–132.
[33] J.-H. Huang, T.-H. Wu, G.-P. Yu, Surf. Coat. Technol. 203 (2009) 3491–3500.
[34] A. Rizzo, M.A. Signore, L. Mirenghi, D. Dimaio, Thin Solid Films 515 (2006) 1486–1493.
[35] K.Y. Cheong, J. Moon, H.J. Kim, W. Bahng, N.-K. Kim, Thin Solid Films 518 (2010) 3255–3259.
[36] Y. Leng, Materials Characterization: Introduction to Microscopic and Spectroscopic Methods, Wiley, Singapore, 2008.
[37] C.D. Wagner, W.M. Riggs, L.E. Davis, J.F. Moulder, G.E. Muilenberg, Handbook of X-ray Photoelectron Spectroscopy: A Reference Book of Standard Data for Use in X-ray Photoelectron Spectroscopy, Physical Electronics Division, Perkin-Elmer Corp., Minnesota, 1979.
[38] J. Koo, Y. Kim, H. Jeon, Jpn. J. Appl. Phys. 41 (2002) 3043–3046.
[39] T.L. Barr, Modern ESCA: The Principles and Practice of X-ray Photoelectron Spectroscopy, CRC Press, 1994.
[40] M. Matsuoka, S. Isotani, J.F.D. Chubaci, S. Miyake, Y. Setsuhara, K. Ogata, N. Kuratani, J. Appl. Phys. 88 (2000) 3773–3775.
[41] M. Del Re, R. Gouttebaron, J.P. Dauchot, P. Leclère, G. Terwagne, M. Hecq, Surf. Coat. Technol. 174/175 (2003) 240–245.
[42] J.M. Howard, N.D. Bassim, V. Craciun, R.K. Singh, Thin Solid Films 453/454 (2004) 411–416.
[43] H.W. Chen, T.Y. Huang, D. Landheer, X. Wu, S. Moisa, G.I. Sproule, T.S. Chao, J. Electrochem. Soc. 149 (2002) F49–F55.
[44] M.J. Guittet, J.P. Crocombette, M. Gautier-Soyer, Phys. Rev. B 63 (2001) 125117.
[45] M.K. Bera, S. Chakraborty, S. Saha, D. Paramanik, S. Varma, S. Bhattacharya, C.K. Maiti, Thin Solid Films 504 (2006) 183–187.
[46] S.J. Wang, C.K. Ong, Appl. Phys. Lett. 80 (2002) 2541–2543.
[47] M.L. Green, E.P. Gusev, R. Degraeve, E.L. Garfunkel, J. Appl. Phys. 90 (2001) 2057–2121.
[48] T. Arantes, G. Mambrini, D. Stroppa, E. Leite, E. Longo, A. Ramirez, E. Camargo, J. Nanopart. Res. 12 (2010) 3105–3110.
[49] H. Shimizu, S. Konagai, M. Ikeda, T. Nishide, Jpn. J. Appl. Phys. 48 (2009) 101101.
[50] H. Young Kim, J. Park, H. Yang, Chem. Phys. Lett. 372 (2003) 269–274.
[51] F. Lu, J. Zhang, M. Huang, F. Namavar, R.C. Ewing, J. Lian, J. Phys. Chem. C 115 (2011) 7193–7201.
[52] J.H. Parker, D.W. Feldman, M. Ashkin, Phys. Rev. 155 (1967) 712.
[53] C.-P.S. Hsu, in: F.A. Settle (Ed.), Handbook of Instrumental Techniques for Analytical Chemistry, Volume 1, The University of Michigan, Prentice Hall, 1997, pp. 247–283.
[54] S. Prati, E. Joseph, G. Sciutto, R. Mazzeo, Accounts Chem. Res. 43 (2010) 792–801.
[55] F. del Monte, W. Larsen, J.D. Mackenzie, J. Am. Ceram. Soc. 83 (2000) 628–634.
[56] A.P. Huang, Z.F. Di, R.K.Y. Fu, P.K. Chu, Surf. Coat. Technol. 201 (2007) 8282–8285.
[57] W. Li, X. Liu, A. Huang, P.K. Chu, J. Phys. D: Appl. Phys. 40 (2007) 2293.
[58] J.J. Yu, I.W. Boyd, Appl. Phys. A: Mater. Sci. Process 75 (2002) 489–491.
[59] G. He, L. Zhang, J. Mater. Sci. Technol. 23 (2007) 433–447.
[60] L.Q. Zhu, Q. Fang, X.J. Wang, J.P. Zhang, M. Liu, G. He, L.D. Zhang, Appl. Surf. Sci. 254 (2008) 5439–5444.
[61] C.S. Zhang, B.J. Flinn, I.V. Mitchell, P.R. Norton, Surf. Sci. 245 (1991) 373–379.
[62] A. Gupta, S. Toby, E.P. Gusev, H.C. Lu, Y. Li, M.L. Green, T. Gustafsson, E. Garfunkel, Prog. Surf. Sci. 59 (1998) 103–115.
[63] T.M. Miller, V.H. Grassian, Catal. Lett. 46 (1997) 213–221.
[64] J. Zhu, S. Albertsma, J.G. van Ommen, L. Lefferts, J. Phys. Chem. B 109 (2005) 9550–9555.
[65] R.H. Petrucci, W.S. Harwood, F.G. Herring, General Chemistry: Principles and Modern Applications, Prentice Hall, 2002, p. p. 795.
[66] A. Lyapin, The Initial Stages of the Oxidation of Zirconium, University of Stuttgart, Germany, 2005.
[67] J.W. Chai, J.S. Pan, Z. Zhang, S.J. Wang, Q. Chen, C.H.A. Huan, Appl. Phys. Lett. 92 (2008) 092119–92123.
[68] H.S. Choi, K.S. Seol, D.Y. Kim, J.S. Kwak, C.-S. Son, I.-H. Choi, Vacuum 80 (2005) 310–316.
[69] M. Filipescu, N. Scarisoreanu, V. Craciun, B. Mitu, A. Purice, A. Moldovan, V. Ion, O. Toma, M. Dinescu, Appl. Surf. Sci. 253 (2007) 8184–8191.
[70] M. Gutowski, J.E. Jaffe, C.-L. Liu, M. Stoker, R.I. Hegde, R.S. Rai, P.J. Tobin, Appl. Phys. Lett. 80 (2002) 1897–1899.
[71] R. Sharma, A. Kumar, J. Anthony, J. Miner. Metals Mater. Soc. (JOM) 53 (2001) 53–55.
[72] G.L.N. Reddy, J.V. Ramana, S. Kumar, S.V. Kumar, V.S. Raju, Appl. Surf. Sci. 253 (2007) 7230–7237.
[73] S.S. Todd, J. Am. Chem. Soc. 72 (1950) 2914–2915.
[74] H.S.C. O'Neill, Am. Miner. 91 (2006) 1134–1141.